HHS Public Access

Author manuscript

Neuroimage. Author manuscript; available in PMC 2023 April 15.

Published in final edited form as:

Neuroimage. 2023 April 15; 270: 119999. doi:10.1016/j.neuroimage.2023.119999.

Using mesoscopic tract-tracing data to guide the estimation of fiber orientation distributions in the mouse brain from diffusion MRI

Zifei Liang,

Tanzil Mahmud Arefin,

Choong H. Lee,

Jiangyang Zhang*

Department of Radiology, Bernard and Irene Schwartz Center for Biomedical Imaging, New York University School of Medicine, 660 First Ave, New York, NY 10016, USA

Abstract

Diffusion MRI (dMRI) tractography is the only tool for non-invasive mapping of macroscopic structural connectivity over the entire brain. Although it has been successfully used to reconstruct large white matter tracts in the human and animal brains, the sensitivity and specificity of dMRI tractography remained limited. In particular, the fiber orientation distributions (FODs) estimated from dMRI signals, key to tractography, may deviate from histologically measured fiber orientation in crossing fibers and gray matter regions. In this study, we demonstrated that a deep learning network, trained using mesoscopic tract-tracing data from the Allen Mouse Brain Connectivity Atlas, was able to improve the estimation of FODs from mouse brain dMRI data. Tractography results based on the network generated FODs showed improved specificity while maintaining sensitivity comparable to results based on FOD estimated using a conventional spherical deconvolution method. Our result is a proof-of-concept of how mesoscale tract-tracing data can guide dMRI tractography and enhance our ability to characterize brain connectivity.

Keywords

Diffusion MRI; Tractography; Mouse brain; Deep learning; Fiber orientation distribution; Connectivity

*Corresponding author. Jiangyang.zhang@nyulangone.org (J. Zhang).

Credit author statement

The project was conceived by Z.L. and J.Z.. T.A. was involved in discussion and tractography. C.L. acquired and analyzed most MR images. Z.L. and J.Z. wrote and prepared the paper, C.L. and T.A. edited the paper.

Declaration of Competing Interest

The authors declare no competing interest related to the work presented here.

Supplementary materials

Supplementary material associated with this article can be found, in the online version, at doi:10.1016/j.neuroimage.2023.119999.

1. Introduction

The introduction of diffusion MRI (dMRI) based tractography more than two decades ago generated great excitement due to its promise of tracing white matter tracts in the brain non-invasively (Basser and Jones, 2002; Jbabdi et al., 2015; Mori and van Zijl, 2002). Aided by increasingly sophisticated dMRI acquisition schemes and tractography methods (Behrens et al., 2007; Frank, 2001; Mori and van Zijl, 2002; Tournier et al., 2007; Tuch et al., 2002; Wedeen et al., 2012, 2008), dMRI tractography had gained the ability to resolve multiple axonal bundles within a voxel as well as high sensitivity to small white matter tracts than the original diffusion tensor imaging-based tractography. To this day, dMRI tractography remains the only tool for non-invasive mapping of macroscopic structural connectivity of the entire brain.

Current routine dMRI tractography starts with the estimation of the fiber orientation distribution (FOD) in each voxel from dMRI signals (Tournier et al., 2007), followed by generation of streamlines connecting neighboring voxels based on FODs using either deterministic or probabilistic algorithms (Behrens et al., 2007; Mori and van Zijl, 2002). While numerous studies in human and animal brains have demonstrated the capabilities of dMRI tractography in visualizing tract trajectories and estimating structural connectivity between brain regions under normal and pathological conditions, e.g. (Catani et al., 2002; Jbabdi et al., 2015; Lo et al., 2010; White et al., 2020), its limitations have also been recognized (Jbabdi and Johansen-Berg, 2011; Jones et al., 2013; Rheault et al., 2020; Schilling et al., 2019), and efforts have been made to understand the underlying causes in order to circumvent or alleviate these limitations.

Numerous studies have compared tractography results with chemical and viral tracer findings from postmortem brain specimens, e.g. (Aydogan et al., 2018; Azadbakht et al., 2015; Calabrese et al., 2015; Chen et al., 2015; Dyrby et al., 2007; Grisot et al., 2021; Howard et al., 2019; Seehaus et al., 2013). While these studies demonstrated good agreements for major white matter tracts, they also revealed noticeable differences when tractography results entered superficial white matter and gray matter regions (Grisot et al., 2021; Howard et al., 2019; Maier-Hein et al., 2017; Reveley et al., 2015; Schilling et al., 2019; Thomas et al., 2014; Wu and Zhang, 2016). Several approaches to improve dMRI tractography have been explored, such as improving spatial resolution (Calabrese et al., 2014; Liebrand et al., 2020; Poot et al., 2013), more accurate estimation of FODs (De Luca et al., 2020; Jeurissen et al., 2014), and optimizing tractography parameters (Fillard et al., 2011; Gutierrez et al., 2020; Moldrich et al., 2010; Schurr et al., 2018).

Among these approaches, the accurate estimation of FOD is of particular importance. Due to its central role in directing tractography. the estimated FODs should closely follow the orientations of underlying axonal pathways. Several studies have compared FODs estimated from dMRI signals with axon orientation distributions measured using a variety of optical techniques including confocal microscopy (Schilling et al., 2016, 2018), polarized light imaging (Mollink et al., 2017), and optical coherence tomography (Jones et al., 2020). These studies generally demonstrated good but not perfect agreements between the estimated

FODs and underlying axonal pathways, echoing the well-recognized challenge of inferring tissue axonal organization from dMRI signals.

In this study, we investigated whether deep learning could improve the estimation of FODs from dMRI signals. While several widely used estimators of FODs are based on dMRI signal models of myelinated axons (Tournier et al., 2007), tissue microstructure in gray matter is more complex than white matter with additional cellular compartments, and our knowledge of how to model dMRI signals from gray matter remains limited. In comparison, the deep learning framework is data-driven and model-free. There have been several reports on using machine and deep learning to predict MRI-based tissue parameters, including FODs, from MRI signals (Gibbons et al., 2019; Li et al., 2021; Lin et al., 2019), by-passing time-consuming model fitting procedures. In particular, Nath et al. demonstrated the use of a deep learning network to learn the relationship between dMRI signals and FODs derived from 3D confocal histology (Nath et al., 2019). Our recent study also demonstrated that the deep learning framework can be used to generate virtual histology from MRI signals by training a network with co-registered MRI and histological data (Liang et al., 2022). With the data from the Allen Mouse Brain Connectivity Atlas (AMBCA) (Kuan et al., 2015; Lein et al., 2007; Oh et al., 2014), which contains a large collection of mouse brain tract-tracing data captured using serial two-photon microscopy, we can now access rich information on mouse brain structural connectivity at the mesoscopic level and use it to guide the estimation of FODs from dMRI signals.

2. Methods

2.1. Generation of a whole brain streamline dataset from AMBCA

The AMBCA used a fast-marching method to generate streamlines that delineate axonal trajectories in each tracer experiment at the mesoscopic level (Fig. 1A–B). The labeling efficiency of the viral tracer used in AMBCA was estimated to be 40–50% (McFarland et al., 2009). The streamlines from 2764 independent experiments were downloaded from AMBCA (http://api.brain-map.org/examples/lines/index.html) and converted from the original JSON format into the TCK format used by MRtrix (www.mrtrix.org) (Tournier et al., 2019). As all the tracer data have been normalized to the Allen Reference Atlas (ARA) space, the streamlines from all experiments were aggregated to form a large streamline dataset (Fig. 1C). As the tracer injection sites in AMBCA experiments were mostly located in one hemisphere, uneven streamline densities between the two hemispheres were observed (Fig. 1C). To resolve this issue, all streamlines were mirrored along the midline of the brain, and the mirrored streamlines were added to the original streamlines to form a symmetric whole brain streamline dataset (Fig. 1D), which contained 3765,678 (~4 million) streamlines. We called this set of streamlines from all experiments the aggregated AMBCA streamlines to distinguish them from streamlines from individual experiments single-experiment (SE) AMBCA streamlines. The aggregated AMBCA streamlines can be downloaded from https://osf.io/m98wn.

2.2. Cell tracing data from the mouseligtht project

To understand the differences between the mesoscopic axonal pathways from AMBCA and the path of individual axon at microscopic level, we compared the SE and aggregated AMBCA streamlines with single cell tracing data from the MouseLight project (Winnubst et al., 2019). The single-cell dataset in the MouseLight project was downloaded from its website (http://ml-neuronbrowser.janelia.org/), which contained reconstructions of 373 long-range projection neurons with axons traveling over long distances and across multiple brain regions. In this dataset, the soma, dendrites, and axons of selected neurons labelled using low-titer viral tracers were traced in serial two-photon microscopy images over the entire brain, presenting axonal pathways at the microscopic level. As the 3D two-photon image volume had been normalized to the ARA space, the downloaded axon tracing data of 373 neurons were converted from the original JSON format into the TCK format used by MRtrix (www.mrtrix.org) and gathered to form the aggregated MouseLight streamlines similar to the generation of the aggregated AMBCA streamlines but without the mirroring step.

2.3. *Ex vivo* mouse brain diffusion MRI

Mouse brain dMRI data were acquired from a separate cohort of animals. All animal experiments have been approved by the Institute Animal Care and Use Committee at New York University. Adult C57BL/6 mice (P56, $n = 10$, 5 M/5F, Charles River, Wilmington, MA, USA) were perfusion fixed with 4% paraformaldehyde (PFA) in PBS. The samples were preserved in 4% PFA for 24 h before transferring to PBS. *Ex vivo* MRI of mouse brain specimens was performed on a horizontal 7 Tesla MR scanner (Bruker Biospin, Billerica, MA, USA) with a triple-axis gradient system. Images were acquired using a quadrature volume excitation coil (72 mm inner diameter) and a receive-only 4-channel phased array cryogenic coil. The specimens were imaged with the skull intact and placed in a syringe filled with Fomblin (perfluorinated polyether, Solvay Specialty Polymers USA, LLC, Alpharetta, GA, USA) to prevent tissue dehydration (Arefin et al., 2021). Three-dimensional diffusion MRI data were acquired using a modified 3D diffusion-weighted gradient- and spin-echo (DW-GRASE) sequence (Aggarwal et al., 2010; Wu et al., 2013) with the following parameters: echo time (TE)/repetition time (TR) = 30/400 ms; two signal averages; field of view (FOV) = 12.8 mm × 10 mm × 18 mm, resolution = 0.1 mm × 0.1 mm × 0.1 mm; two non diffusion weighted images (b_0s); 60 diffusion weighted images (DWIs) with a diffusion weighting (b) of 5000 s/mm^2.

From the dMRI data, diffusion tensors were calculated using the loglinear fitting method implemented in MRtrix (http://www.mrtrix.org) at each pixel, and maps of mean and radial diffusivities and fractional anisotropy were generated. FOD maps were generated using constrained spherical deconvolution (CSD) implemented in MRtrix using a single response function estimated from white matter structures as described in (Arefin et al., 2021). Mappings between individual MRI data and the ARA space were computed using the Large Deformation Diffeomorphic Metric Mapping (LDDMM) (Miller et al., 2002) implemented in the DiffeoMap software (www.mristudio.org) as described in (Ceritoglu et al., 2009; Lim et al., 2013).

2.4. Estimation of tract-orientation-distribution (TOD) from the streamline dataset

The aggregated AMBCA streamlines were mapped from the ARA space to each subject using the mappings generated using LDDMM, which were diffeomorphic (one-to-one and differentiable) and allowed us to transform the AMBCA streamlines without changing the topology of the streamline networks. We chose this route instead of mapping dMRI data into the ARA space because the dMRI data were associated with the diffusion encoding directions used during acquisition and estimation of FODs from nonlinear mapped dMRI data requires voxel-wise adjustments of the diffusion encoding directions and amplitude, which was not a trivial task.

A 3D TOD map was then generated from the aggregated AMBCA streamlines mapped into individual subject space using the tckmap command in MRtrix with the maximum spherical harmonic degree (lmax) set to 6 (Dhollander et al., 2014). The orientation and amplitude of the TOD reflected the arrangement and number of AMBCA streamlines at each voxel after mapping. Using the initial TODs, we computed short streamlines with lengths less than 6 mm and then generated the so-called level-2 TODs based on the short streamlines as described in (Dhollander et al., 2014). As the amplitudes of TODs generated from the aggregated AMBCA streamlines depend on the distribution of injection sites and may not reflect the actual number of axons, the amplitudes of the 28 TOD coefficients were normalized at each voxel by L_1 norm. We called the normalized TODs the AMBCA TODs (Fig. 1E).

2.5. Deep learning neural network to predict FODs from dMRI signals

We started with a network described in (Lin et al., 2019), which was trained to predict CSD-FODs from dMRI signals. Briefly, the network consisted of two convolutional layers ($2 \times 2 \times 2$ kernel, 1024 and 512 filters, respectively), two fully connected layers (512 and 256 nodes, respectively), and one output layer. The inputs to the network were $3 \times 3 \times 3$ voxel patches from dMRI data as in (Lin et al., 2019), with each voxel containing 60 diffusion-weighted signals normalized by the average of the two non-diffusion-weighted signals. The outputs of the network were 28 CSD-FOD coefficients. The network was implemented in Python using Keras (www.github.com/fchollet/keras), and the training was performed on a desktop GPU (NVIDIA RTX 2080). MRI data from 10 subjects were randomly assigned to training ($n = 6$) and testing ($n = 4$) groups. One million $3 \times 3 \times 3$ patches from the training mouse brain dMRI data and their corresponding CSD-FODs were used for training, within which 10% was used as the validation cohort. We used the same hyper-parameter setting as described in (Lin et al., 2019): network weights initialization by truncated normal distribution centered on 0; initial learning rate = $1e^{-4}$, beta1 = 0.9, beta2 = 0.999, epsilon = $1e^{-08}$; Momentum = 0.5; Number of epochs = 1000; Batch size = 512. We employed the commonly used Adam's method (Duchi et al., 2011) to stochastically optimize a mean squared error loss function with some hyper-parameters assigned before training. Early stopping was also employed by monitoring whether the validation set loss stabilized within 50 epochs to prevent overfitting (Zur et al., 2009). Using the testing data as inputs to the trained network, the predicted FODs agreed well with CSD-FODs estimated from the same data using MRtrix (Supplementary Fig. 1).

2.6. Deep learning neural network to predict TODs from dMRI signals

Compared to predicting CSD-FODs from dMRI data, predicting AMBCA TODs from dMRI data faced additional challenges due to the residual mismatches between MRI and AMBCA TOD data, as well as potential discrepancies at the voxel level between the AMBCA TODs, which was computed based on the number of the aggregated AMBCA streamlines and not necessarily the actual number of axons, and dMRI signals, which reflected the actual microstructural organization (e.g. axons) in the mouse brain. To address these issues, we used a modified network as shown in Fig. 2. Compared to the network introduced by Lin et al. (2019), we kept the first two convolutional layers (2 × 2 × 2 kernel) but increased the number of filters to 1024 for both layers. We increased the number of fully connected layers from 2 to 3 with 1024, 512, and 256 nodes. We also added 40% random dropout (Demsar and Zupan, 2021; Srivastava et al., 2014; Ying, 2019) in the two convolutional layers and the first fully connected layer as a regularization during network training. In addition, we replaced the ReLU in the hidden layers with the Parametric Rectified linear unit (PReLU) that modulates the node output (y = x, when $x > 0$; y = axe, when $x < 0$; where a is a trainable parameter) to introduce nonlinear functions that can over-come the so-called dying ReLU problem (He et al., 2015). Here, we kept the 3 × 3 × 3 patch size unchanged because we assumed that the relationship between dMRI signals and axonal bundles in the same voxel should be local and independent of neighboring voxels. Different from (Lin et al., 2019), there was residual mismatches between input dMRI data and target TOD maps, which can be accommodated by the 3 × 3 × 3 patch size as suggested by our previous report (Liang et al., 2022). We increased the training data to 3 million patches to avoid over-fitting.

During training, all hyper-parameters were initialized in the same way as described in Section 2.5 with a mean squared error loss function. Training was carried out using an NVIDIA RTX 2080Ti and occupied 22 GB out of the total 24GB of memory with three million voxels. Since the network performed on relatively small 3 × 3 × 3 patches, it used less than 250 MB memory for voxel-wise TOD prediction. It took approximately 30 min to estimate a 3D DL-TOD map from a dMRI volume with a size of 256 × 200 × 300. The trained models and codes are available at (https://github.com/liangzifei/MRTod_net). The output of the TODNet was called deep learning TODs (DL-TODs).

2.7. Tractography

Whole brain probabilistic tractography based on CSD-FODs or DL-TODs were performed using the tckgen command in MRtrix (v 3.0.3) with the FOD2 option and the optimized parameters reported in (Aydogan et al., 2018): turning angle < 45°, minimal/maximal length = 0.3/23 mm, FOD amplitude threshold = 0.1. It took approximately 2 h to generate four million streamlines on a PC workstation (Intel Xeon E5–1650, 3.6 GHz, 64GB of RAM). The tractography streamlines were then mapped from individual subject space to the ARA space using the mappings generated in Section 2.3.

From ten selected AMBCA experiments, the injection regions, which had strong intensity values, were manually defined in the tract tracing data. From the whole brain tractography streamlines mapped to the ARA space, we selected streamlines that passed through the injection regions and converted the streamline data to binary images (voxel value set to 1

if one or more streamlines passed through the voxel and 0 otherwise) for each injection region. Similarly, streamlines were selected from the aggregated AMBCA streamlines and converted to binary images, which were then dilated by 1 voxel to match the extent of axon projections in the native tracer results (Fig. 1B). For each subject and injection region, we used the DICE value of the binary images from tracer and tractography streamlines to quantify their spatial agreement.

2.8. Generation of a digital phantom

Simulated dMRI signals of crossing fibers were generated using a two-tensor model

$$\frac{S}{S_0} = f \cdot \exp\left(-bg^T D_1 g\right) + (1-f) \cdot \exp\left(-bg^T D_2 g\right) \quad (1)$$

where S and S_0 are diffusion-weighted and non-diffusion-weighted signals, f the volume fraction, D_1 and D_2 the diffusion tensors, and b and g the diffusion weighting and encoding direction, respectively. In this study, we chose 12 sets of eigen values for D_1 and D_2 (Table 1 and Supplementary Fig. 2), ranging from isotropic diffusion to highly anisotropic diffusion, based on our *Ex vivo* mouse brain dMRI data. A 6 × 6 digital phantom was created by combining different D_1 and D_2 with $f = 0.5$. We used the same diffusion weighting and diffusion encoding vectors as used in our dMRI acquisition. Simulated dMRI signals with various volume fraction (f) were generated using Matlab (Math-works Inc. Natick, MA, USA) to compare estimated CSD-FODs and DL-TODs.

2.9. Statistical analysis

Two-sample paired t-test was used to test whether there was significant angular difference between the primary orientation of AMBCA TODs and CSD-FODs or DL-TODs from dMRI (corrections for multiple comparisons with false discovery rate = 0.1, GraphPad Prism 9.0, www.GraphPad.com) Two-sample paired t-test with corrections for multiple comparisons was also used to test whether there was significant difference in DICE values between binary image volumes from selected AMBCA streamlines and CSD-FOD/DL-TOD tractography results as described in Section 2.7.

3. Results

3.1. The whole brain tracer streamline dataset

The aggregated AMBCA streamlines, which included data from multiple injection experiments, visualized the dense axonal pathways throughout the mouse forebrain. Major white matter tracts, such as the corpus callosum, anterior commissure, can be delineated in the dataset (Fig. 3A). Coherently arranged streamlines were also found in gray matter regions (e.g. cortex and hippocampus), reflecting axonal pathways in those regions, which are often challenging to reconstruct using dMRI tractography.

We then compared SE AMBCA streamlines, which consist of anterograde streamlines originated from an injection region, with streamlines selected using the same injection region from the aggregated AMBCA and MouseLight streamlines (i.e. streamlines that passed through the injection region) (Fig. 3B–C). The SE AMBCA streamlines generally

agreed with the selected MouseLight streamlines (e.g. Fig. 3B) but differences did emerge. For example, in Fig. 3C, the SE AMBCA streamlines showed connections to the contralateral hemisphere, whereas the selected MouseLight streamlines did not cross the midline but reached more regions within the ipsilateral hemisphere. These differences came from the fact that the MouseLight streamlines are long-range axonal projections of sparsely sampled individual neurons at the single cell level from cell tracing, whereas AMBCA streamlines represent bundles of axons at the mesoscopic level from groups of labeled neurons in the injection region.

Compared to the SE AMBCA streamlines, the selected aggregated AMBCA streamlines from the same injection region included additional streamlines that reached more regions. These additional streamlines potentially came from three sources: (1) retrograde streamlines originated from other regions but ended in the injection region; (2) streamlines that merely passed through the injection region; (3) variations in SE streamlines due to individual as well as inter-experimental variations. Compared to the selected aggregated MouseLight streamlines, the selected aggregated AMBCA streamlines from the same injection region also showed more extensive reach, and the two set of streamlines showed consistent trajectories (Fig. 3B–C), suggesting the aggregated AMBCA streamlines captured the major forebrain axonal pathways within the MouseLight data.

3.2. A comparison of the AMBCA streamline data with dMRI tractograophy

Remarkable differences were found between the aggregated AMBCA streamlines and whole brain dMRI tractography streamlines from *Ex vivo* mouse brains. With the same number of total streamlines (4 million), the aggregated AMBCA streamline density maps showed less gray and white matter contrasts than streamline density maps from dMRI tractography (Fig. 3D), suggesting that tractography streamlines generated from CSD-FODs estimated here (based on dMRI data acquired here and using single white matter response function) tended to stay within white matter regions. The overall contrast pattern found in the aggregated AMBCA streamline density map resembled neurofilament stained histological sections (Fig. 3D), in which signal intensities reflect axonal density. In addition, the AMBCA streamlines tended to be longer than dMRI tractography streamlines (Fig. 3E).

3.3. TODNet can predict tracer streamline TOD

As expected, the DL-TOD maps generated by the TODNet based on dMRI data from the test group resembled the AMBCA TOD maps (Fig. 4A). In large white matter structures (e.g. the corpus callosum), the AMBCA TODs, DL-TODs, and CSD-FODs had narrow lobes along the orientations of fibers. In gray matter structures (e.g. the cortex), the CSD-FOD results showed multiple distinct lobes, whereas the AMBCA TODs and DL-TODs had no clearly defined lobes (Fig. 4A), making direct comparisons of DL-TODs and CSD-FODs difficult. We measured the differences in the primary orientation (the orientation of the lobe with the highest amplitude) between DL-TODs and AMBCA TODs and between CSD-FODs and AMBCA TODs at each voxel in each subject space (Fig. 4B). In white matter regions, DL-TODs were slightly better aligned to the AMBCA TODs than CSD-FODs (8.54° vs 12.94°, $p < 0.0001$, $n = 4$). In gray matter regions, DL-TODs showed much reduced angular

difference compared to AMBCA TODs than CSD-FODs (Fig. 3C; 35.24° vs 53.16°, $p < 0.0001$, $n = 4$), notably in the cortex and hippocampus (Fig. 4B).

We compared DL-TODs with CSD-FODs with respect to AMBCA TODs in the mouse cortex and hippocampus. In the sensory cortex, the aggregated AMBCA streamlines showed tangential streamlines (parallel to the cortical surface) in the top and bottom regions of the cortex (Fig. 5A, white and yellow arrows). This arraignment was reproduced by the primary orientations of DL-TODs, but not by the primary orientation of CSD-FODs, which showed a uniform radial organization throughout the cortex (Fig. 5).

In the hippocampus, the aggregated AMBCA streamlines mostly ran along the left-right (red) or anterior-posterior (green) orientations. The primary orientations of DL-TODs mostly agreed with the AMBCA streamlines (red and green), but the primary orientations of CSD-FODs were along the dorsal-ventral orientation (blue) (Fig. 6A). The orientations of the aggregated AMBCA streamlines in the hippocampus were confirmed by the MouseLight dataset. With a few exceptions, axons in the CA1 region of the mouse hippocampus in the MouseLight dataset, either from neurons in the CA1 region or from other parts of the hippocampus, have left-right and anterior-posterior orientations (Fig. 6C,E–H), matching the AMBCA streamline results (Fig. 6A). In comparison, dense dendritic networks of the CA1 neurons (Fig. 6D) from the MouseLight dataset were organized along dorsal-ventral orientation, along the primary directions of CSD-FODs.

3.4. DL-TOD based tractography in the mouse brain

We then examined whether DL-TOD was able to improve tractography in the mouse brain. As explained in Section 3.1, the aggregated AMBCA streamlines potentially captured all axonal pathways passing through a region, not just the anterograde pathways originated from it (as in SE AMBCA streamlines). It is therefore appropriate to compare tractography results starting from a seed region with aggregated AMBCA streamlines that passed the same region.

Using a set of ten injection regions in the AMBCA, located throughout the mouse forebrain, streamlines that passed through these regions were selected from the aggregated AMBCA streamlines as well as whole brain tractography results based on CSD-FODs and DL-TODs. Visually, tractography results based on DL-TODs agreed with the selected AMBCA streamlines better than tractography results based on CSD-FODs (Fig. 7A–C). We then used the dice index to measure spatial agreements between tractography results and the selected aggregated AMBCA streamlines from the ten regions (Fig. 7D). The DL-TOD results had significantly higher DICE scores than the CSD-FOD results in 7 out of the 10 cases and comparable DICE scores for the rest. Further analysis showed that DL-TOD based tractography improved specificity by reducing overreach, while mostly maintaining a comparable level of sensitivity or overlap compared to FOD-based tractography. In Fig. 7E, the DL-TOD-based tractography results, represented by maroon symbols, were mostly to the left of the CSD-FOD-based tractography results, represented by blue symbols. Among the 10 regions, one region in the cortex (ID# 309372716, with injection site located in the primary visual cortex) showed a large drop in sensitivity in DL-TOD-based tractography compared to CSD-FOD based tractography.

3.5. Potential effects of streamline distribution in AMBCA on DL-TOD

Based on the dMRI signals in the corpus callosum, we simulated dMRI signals from orthogonal crossing fibers, as shown by the estimated CSD-FODs (Fig. 8A). In the six-by-six matrix, CSD-FODs along the upper or left edge only had one pair of lobes, representing voxels with a single group of fibers, and CSD-FODs in other places showed two lobes with equal amplitudes, representing the crossing of two groups of fibers. The estimated DL-TODs from the simulated dMRI signals showed less sharply defined lobes than CSD-FODs (Fig. 8A). When fibers along the x axis (left-right in the mouse brain) were mixed with fibers along the z axis (rostral-caudal in the mouse brain), the estimated DL-TODs showed more preference for the x axis than the z axis, as the DL-TODs in the diagonal elements have their primary orientations along the x axis. When fibers along the x axis were mixed with fibers along the y axis (dorsal-ventral in the mouse brain), the estimated DL-TODs showed more preference for the y axis than the x axis.

The preference toward certain orientations in the DL-TODs might reflect the distribution of orientation in the AMBCA streamline dataset. When we projected the orientation of each streamline segment onto the x, y, and z axes, the projections along the y axis out-numbered the projections along the other two axes (Fig. 8B), which might have caused the tilt toward the y axis, followed by the x axis, of DL-TODs. Furthermore, examinations of the angles between each streamline segments and the x/y/z axis showed that, among the streamline segments that closely aligned with the x, y, and z axes (angle <10°), there are more streamlines segments closely aligned with the x axis than with the other two axes (Fig. 8C). This might explain why the DL-TODs in the simulation were sharper for fiber groups along the x axis than others.

4. Discussion

While this study has shown that a deep learning network trained with mesoscopic tract-tracing data can enhance the accuracy of FOD estimation from mouse brain dMRI data, the potential of such networks to improve the mapping of structural connectivity in the mouse and eventually the human brain hinges on our ability to acquire comprehensive ground truth tract-tracing data and generalize the network to other species.

4.1. The advantages and limitations of the aggregated AMBCA streamlines

Even though the importance of validating tractography using histological ground truth has long been recognized (Azadbakht et al., 2015; Dyrby et al., 2007; Gutierrez et al., 2020; Lin et al., 2001; Schilling et al., 2018; Seehaus et al., 2013; Thomas et al., 2014), suitable ground truth data for this purpose has not yet been available. Previous studies on validation and optimization of dMRI based FOD estimation mostly used local microscopy measurements as ground truth (Mollink et al., 2017; Schilling et al., 2016, 2018). Obtaining comprehensive data on axonal pathways at the mesoscopic or microscopic levels over the entire brain is still technically challenging and time consuming. For example, the connectome of the adult drosophila brain was completed only recently (Scheffer et al., 2020). The aggregated AMBCA streamlines, which combine streamlines from multiple experiments and are therefore more comprehensive than individual tract tracing experiments,

may be a suitable candidate for validation and optimization of FOD estimation and dMRI tractography. Although it would be ideal to have dMRI and tract tracing data from the same animals as suggested by previous studies (Grisot et al., 2021), it is impractical to re-acquire a comprehensive collection of tracer results using methods based on viral or chemical tracers. This study was therefore based on two assumptions: (1) the aggregated AMBCA streamlines, with data from more than 2700 subjects, captured common forebrain axonal pathways in the C57BL/6 mouse forebrain; and (2) the inter-subject differences among the inbred C57BL mouse brains were small that comparisons between the aggregated AMBCA streamlines and dMRI signals acquired from a separate cohort of C57BL/6 mice at the same age as the mouse brains in AMBCA can be performed after proper registration.

Although it is difficult to confirm the first assumption, evidence from comparing the aggregated AMBCA streamlines with cell tracing results from the MouseLight projects (Fig. 3B–C) suggests that at least the axonal pathways in the cortex and hippocampus were well covered. The aggregated AMBCA streamlines, however, remained an incomplete representation of the axonal networks in the mouse brain in several other aspects due to several limitations, including non-uniform distribution of injection sites, varying dosages and labeling efficiency, imaging resolution, and the fast-marching algorithm. For example, as the cerebellum received fewer injections than the cortex, the density of streamlines in the cerebellum was noticeably lower than in the forebrain as shown in Fig. 2D. Due to this reason, although the orientations of TODs should mostly reflect those of actual axonal pathways, the amplitudes of the AMBCA TODs were not used in this study. This limitation may be alleviated with more tract and cell tracing resources in the future (e.g. (Winnubst et al., 2019; Zingg et al., 2014)). It is also not clear whether the technique developed using the aggregated AMBCA streamlines can be translated to data from the human brain, due to the vast differences in imaging resolution as well as differences in microstructural organization. The recent reports of tract tracing in non-human primate brain (Charvet et al., 2022; Howard et al., 2019; Xu et al., 2021) offer hope that such data, which have higher translational value, may become more readily available in the future. For the second assumption to hold, it is necessary to image a large number of subjects, more than the number of subjects in this study so that impacts of individual variations in microstructural organization including axonal pathways will be reduced.

4.2. Deep learning can enhance the estimation of FOD

The deep learning framework has several advantages that complement existing modeling approaches, as it is data-driven and not limited by underlying assumptions associated with models. Here, we trained out network using small $3 \times 3 \times 3$ patches instead of entire images because we assumed the relationship between dMRI signals and underlying axonal pathways to be strictly local (i.e. MRI signals are the ensemble average of spins within each voxel and do not depend on neighboring voxels) and would like to limit the amount of spatial information available to the network, in a similar fashion as our previous study connecting MRI signals and histology (Liang et al., 2022). As a result, a limited number of typical dMRI data, instead of thousands as required in typical deep learning studies, can provide sufficient instances to train the deep learning network to resolve the orientation of certain axonal pathways in gray matter. The network can be extended to include

dMRI data acquired using optimized parameters or other MRI contrasts to further enhance its capability. For example, the recent developments on the multi-dimensional diffusion encoding (Topgaard, 2017) may provide critical information on tissue microstructural organization that can be utilized by the network.

Our results demonstrated that deep learning networks, trained with tract tracing data, were able to improve the estimation of FODs (Figs. 5 and 6) and tractography (Fig. 7) in the mouse brain. This is in line with results reported by Nath et al. (Nath et al., 2019). The improvements were most obvious in gray matter regions (Fig. 4B–C) since conventional CSD-FODs are already fairly accurate in depicting the orientation of white matter bundles (Lin et al., 2001; Mollink et al., 2017; Schilling et al., 2018). The complex microstructural organization in gray matter, with the presence of dendritic networks and other cellular compartments, however, challenges the power of dMRI in resolving axonal pathways in gray matter regions, as shown previously in the mouse hippocampus (Wu and Zhang, 2016) and other regions (Moldrich et al., 2010; Ren et al., 2007; Wu et al., 2014). The deep learning network developed here, as shown in Fig. 6, may be used to reconstruct structural connectivity in the mouse hippocampus or other regions.

One challenge introduced by AMBCA TODs was that, while AMBCA TODs in large white matter tracts had sharp lobes that aligned with CSD-FODs, AMBCA TODs in gray matter regions (e.g. the cortex) tended to have less well-defined FOD lobes (Figs. 4 and 5). This potentially reflected the large dispersion of streamlines in these regions, which is different from the assumption behind the estimation of CSD-FODs using a single response function based on dMRI signals from white matter structures. We did not compare our results with recent work on developing more accurate estimation of FODs in gray matter region (De Luca et al., 2020; Jeurissen et al., 2014), which should be considered for future studies.

The deep leaning method used in our work still has room for improvement. For example, the MSE loss function used in training the network may not be optimal as it assigned equal weighting to all 28 TOD spherical harmonic coefficients. As some TOD coefficients can have much higher amplitudes than others, the loss function used here may have introduced a bias for high amplitude coefficients. One solution is to use multiple loss functions (Ghodrati et al., 2019; Kendall et al., 2018; Wang et al., 2022), which should be explored in future studies. Another limitation of the deep learning approach here is that biases in the training data will influence the network predictions. The mouse brain has a higher relative gray matter volume than the human brain. In addition, the distribution of streamlines' orientation, as shown in Fig. 8B, was not uniform, which may reflect actual axonal organization in the brain (i.e. more axons running horizontally than axons running vertically) or may be a result of the atlas space used here. In the future, training datasets containing with equalized tissue types and multiple orientations may be able to reduce the bias.

Our results also did not provide detailed knowledge of the inner working of the network. For example, it is intriguing that the network was able to assign distinct orientations to the superficial, middle, and deep cortical regions based on dMRI signals (Fig. 5). The normalized dMRI signals in these three regions and corpus callosum are displayed in Fig. 9. The dMRI signals from the three cortical regions all showed higher degrees of attenuation

than signals from the corpus callosum, except when the diffusion encoding gradients were close to the left-right direction (polar angle close to 0 and $\pm\pi$ in the plot). Close examinations revealed different patterns among the three cortical regions. For instance, signals from the superficial and deep cortical regions showed less attenuation along certain directions (area 2 in Fig. 9) but more attenuation along other directions (area 1 in Fig. 9) than signals from the middle cortical region, potentially due to different fiber orientations. The deep learning network might have recognized the differences in dMRI signals among the three regions and used the information to predict the DL-TOD, whereas the conventional CSD methods using a single response function derived from white matter regions did not resolve the fiber orientations accurately in this case.

In summary, we demonstrated that a deep learning network, trained using the aggregated AMBCA streamline, can improve the estimation of FODs as well as the specificity of tractography from mouse brain dMRI data. The technique developed here can be used to characterize structural connectivity in the mouse brain.

Supplementary Material

Refer to Web version on PubMed Central for supplementary material.

Acknowledgement

This work was supported by NIH grants R01NS102904 and R01HD074593. The majority of this work was performed at the NYU Langone Health Preclinical Imaging Laboratory, a shared resource partially supported by the NIH/SIG 1S10OD018337-01, the Laura and Isaac Perlmutter Cancer Center Support Grant, NIH/NCI 5P30CA016087, and the NIBIB Biomedical Technology Re-source Center Grant NIH P41 EB017183 as well as by the NYU CTSA grant UL1 TR000038 from the National Center for Advancing Translational Sciences, National Institutes of Health.

Data and materials availability

The analyses in this study were carried out on publicly available datasets. The mouse brain streamline data were obtained from the Allen mouse connectivity project (http://connectivity.brain-map.org). Code and data for training are available at https://github.com/liangzifei/MR-TOD-net. The aggregated AMBCA streamlines can be downloaded from https://osf.io/m98wn.

Data Availability

Data will be made available on request.

References

Aggarwal M, Mori S, Shimogori T, Blackshaw S, Zhang JY, 2010. Three-dimensional diffusion tensor microimaging for anatomical characterization of the mouse brain. Magn. Reson. Med 64, 249–261. [PubMed: 20577980]

Arefin TM, Lee CH, White JD, Zhang J, Kaffman A, 2021. Macroscopic structural and connectome mapping of the mouse brain using diffusion magnetic resonance imaging. Bio Protoc. 11, e4221.

Aydogan DB, Jacobs R, Dulawa S, Thompson SL, Francois MC, Toga AW, Dong HW, Knowles JA, Shi YG, 2018. When tractography meets tracer injections: a systematic study of trends and variation sources of diffusion-based connectivity. Brain Struct. Funct 223, 2841–2858. [PubMed: 29663135]

Azadbakht H, Parkes LM, Haroon HA, Augath M, Logothetis NK, de Crespigny A, D'Arceuil HE, Parker GJM, 2015. Validation of high-resolution tractography against *in vivo* tracing in the macaque visual cortex. Cereb. Cortex 25, 4299–4309. [PubMed: 25787833]

Basser PJ, Jones DK, 2002. Diffusion-tensor MRI: theory, experimental design and data analysis - a technical review. NMR Biomed. 15, 456–467. [PubMed: 12489095]

Behrens TE, Berg HJ, Jbabdi S, Rushworth MF, Woolrich MW, 2007. Probabilistic diffusion tractography with multiple fibre orientations: what can we gain? NeuroimageNeuroimage 34, 144–155.

Calabrese E, Badea A, Coe CL, Lubach GR, Styner MA, Johnson GA, 2014. Investigating the tradeoffs between spatial resolution and diffusion sampling for brain mapping with diffusion tractography: time well spent? Hum. Brain Mapp 35, 5667–5685. [PubMed: 25044786]

Calabrese M, Magliozzi R, Ciccarelli O, Geurts JJG, Reynolds R, Martin R, 2015. Exploring the origins of grey matter damage in multiple sclerosis. Nat. Rev. Neurosci 16, 147–158. [PubMed: 25697158]

Catani M, Howard RJ, Pajevic S, Jones DK, 2002. Virtual *in vivo* interactive dissection of white matter fasciculi in the human brain. Neuroimage 17, 77–94. [PubMed: 12482069]

Ceritoglu C, Oishi K, Li X, Chou MC, Younes L, Albert M, Lyketsos C, van Zijl PC, Miller MI, Mori S, 2009. Multi-contrast large deformation diffeomorphic metric mapping for diffusion tensor imaging. Neuroimage 47, 618–627. [PubMed: 19398016]

Charvet CJ, Ofori K, Baucum C, Sun J, Modrell MS, Hekmatyar K, Edlow BL, van der Kouwe AJ, 2022. Tracing modification to cortical circuits in human and nonhuman primates from high-resolution tractography, transcription, and temporal dimensions. J. Neurosci 42, 3749–3767. [PubMed: 35332086]

Chen H, Liu T, Zhao Y, Zhang T, Li Y, Li M, Zhang H, Kuang H, Guo L, Tsien JZ, Liu T, 2015. Optimization of large-scale mouse brain connectome via joint evaluation of DTI and neuron tracing data. Neuroimage 115, 202–213. [PubMed: 25953631]

De Luca A, Guo F, Froeling M, Leemans A, 2020. Spherical deconvolution with tissue-specific response functions and multi-shell diffusion MRI to estimate multiple fiber orientation distributions (mFODs). Neuroimage 222, 117206. [PubMed: 32745681]

Demsar J, Zupan B, 2021. Hands-on training about overfitting. PLoS Comput. Biol 17.

Dhollander T, Emsell L, Van Hecke W, Maes F, Sunaert S, Suetens P, 2014. Track orientation density imaging (TODI) and track orientation distribution (TOD) based tractography. Neuroimage 94, 312–336. [PubMed: 24389015]

Duchi J, Hazan E, Singer Y, 2011. Adaptive subgradient methods for online learning and stochastic optimization. J. Mach. Learn. Res 12, 2121–2159.

Dyrby TB, Sogaard LV, Parker GJ, Alexander DC, Lind NM, Baare WF, Hay-Schmidt A, Eriksen N, Pakkenberg B, Paulson OB, Jelsing J, 2007. Validation of *in vitro* probabilistic tractography. Neuroimage 37, 1267–1277. [PubMed: 17706434]

Fillard P, Descoteaux M, Goh A, Gouttard S, Jeurissen B, Malcolm J, Ramirez-Manzanares A, Reisert M, Sakaie K, Tensaouti F, Yo T, Mangin JF, Poupon C, 2011. Quantitative evaluation of 10 tractography algorithms on a realistic diffusion MR phantom. Neuroimage 56, 220–234. [PubMed: 21256221]

Frank LR, 2001. Anisotropy in high angular resolution diffusion-weighted MRI. Magn. Reson. Med 45, 935–939. [PubMed: 11378869]

Ghodrati V, Shao J, Bydder M, Zhou Z, Yin W, Nguyen KL, Yang Y, Hu P, 2019. MR image reconstruction using deep learning: evaluation of network structure and loss functions. Quant. Imaging Med. Surg 9, 1516–1527. [PubMed: 31667138]

Gibbons EK, Hodgson KK, Chaudhari AS, Richards LG, Majersik JJ, Adluru G, DiBella EVR, 2019. Simultaneous NODDI and GFA parameter map generation from subsampled q-space imaging using deep learning. Magn. Reson. Med 81, 2399–2411. [PubMed: 30426558]

Grisot G, Haber SN, Yendiki A, 2021. Diffusion MRI and anatomic tracing in the same brain reveal common failure modes of tractography. Neuroimage 239.

Gutierrez CE, Skibbe H, Nakae K, Tsukada H, Lienard J, Watakabe A, Hata J, Reisert M, Woodward A, Yamaguchi Y, Yamamori T, Okano H, Ishii S, Doya K, 2020. Optimization and validation of diffusion MRI-based fiber tracking with neural tracer data as a reference. Sci. Rep 10.

He KM, Zhang XY, Ren SQ, Sun J, 2015. Delving deep into rectifiers: surpassing human-level performance on imagenet classification. In: Proceedings of the IEEE International Conference on Computer Vision (Iccv), pp. 1026–1034.

Howard AF, Mollink J, Kleinnijenhuis M, Pallebage-Gamarallage M, Bastiani M, Cottaar M, Miller KL, Jbabdi S, 2019. Joint modelling of diffusion MRI and microscopy. Neuroimage 201, 116014. [PubMed: 31315062]

Jbabdi S, Johansen-Berg H, 2011. Tractography: where do we go from here? Brain Connect. 1, 169–183. [PubMed: 22433046]

Jbabdi S, Sotiropoulos SN, Haber SN, Van Essen DC, Behrens TE, 2015. Measuring macroscopic brain connections *in vivo*. Nat. Neurosci 18, 1546–1555. [PubMed: 26505566]

Jeurissen B, Tournier JD, Dhollander T, Connelly A, Sijbers J, 2014. Multi-tissue constrained spherical deconvolution for improved analysis of multi-shell diffusion MRI data. Neuroimage 103, 411–426. [PubMed: 25109526]

Jones DK, Knosche TR, Turner R, 2013. White matter integrity, fiber count, and other fallacies: the do's and don'ts of diffusion MRI. Neuroimage 73, 239–254. [PubMed: 22846632]

Jones R, Grisot G, Augustinack J, Magnain C, Boas DA, Fischl B, Wang H, Yendiki A, 2020. Insight into the fundamental trade-offs of diffusion MRI from polarization-sensitive optical coherence tomography in *ex vivo* human brain. Neuroimage 214.

Kendall A, Gal Y, Cipolla R, 2018. Multi-task learning using uncertainty to weigh losses for scene geometry and semantics. In: Proceedings of the IEEE Conference on Computer Vision and Pattern Recognition, pp. 7482–7491.

Kuan L, Li Y, Lau C, Feng D, Bernard A, Sunkin SM, Zeng H, Dang C, Hawrylycz M, Ng L, 2015. Neuroinformatics of the allen mouse brain connectivity atlas. Methods 73, 4–17. [PubMed: 25536338]

Lein ES, Hawrylycz MJ, Ao N, Ayres M, Bensinger A, Bernard A, Boe AF, Boguski MS, Brockway KS, Byrnes EJ, Chen L, Chen L, Chen TM, Chin MC, Chong J, Crook BE, Czaplinska A, Dang CN, Datta S, Dee NR, Desaki AL, Desta T, Diep E, Dolbeare TA, Donelan MJ, Dong HW, Dougherty JG, Duncan BJ, Ebbert AJ, Eichele G, Estin LK, Faber C, Facer BA, Fields R, Fischer SR, Fliss TP, Frensley C, Gates SN, Glattfelder KJ, Halverson KR, Hart MR, Hohmann JG, Howell MP, Jeung DP, Johnson RA, Karr PT, Kawal R, Kidney JM, Knapik RH, Kuan CL, Lake JH, Laramee AR, Larsen KD, Lau C, Lemon TA, Liang AJ, Liu Y, Luong LT, Michaels J, Morgan JJ, Morgan RJ, Mortrud MT, Mosqueda NF, Ng LL, Ng R, Orta GJ, Overly CC, Pak TH, Parry SE, Pathak SD, Pearson OC, Puchalski RB, Riley ZL, Rockett HR, Rowland SA, Royall JJ, Ruiz MJ, Sarno NR, Schaffnit K, Shapovalova NV, Sivisay T, Slaughterbeck CR, Smith SC, Smith KA, Smith BI, Sodt AJ, Stewart NN, Stumpf KR, Sunkin SM, Sutram M, Tam A, Teemer CD, Thaller C, Thompson CL, Varnam LR, Visel A, Whitlock RM, Wohnoutka PE, Wolkey CK, Wong VY, Wood M, Yaylaoglu MB, Young RC, Youngstrom BL, Yuan XF, Zhang B, Zwingman TA, Jones AR, 2007. Genome-wide atlas of gene expression in the adult mouse brain. Nature 445, 168–176. [PubMed: 17151600]

Li H, Liang Z, Zhang C, Liu R, Li J, Zhang W, Liang D, Shen B, Zhang X, Ge Y, Zhang J, Ying L, 2021. SuperDTI: ultrafast DTI and fiber tractography with deep learning. Magn. Reson. Med 86, 3334–3347. [PubMed: 34309073]

Liang Z, Lee CH, Arefin TM, Dong Z, Walczak P, Shi SH, Knoll F, Ge Y, Ying L, Zhang J, 2022. Virtual mouse brain histology from multi-contrast MRI via deep learning. eLife 11.

Liebrand LC, van Wingen GA, Vos FM, Denys D, Caan MWA, 2020. Spatial versus angular resolution for tractography-assisted planning of deep brain stimulation. Neuroimage Clin. 25, 102116. [PubMed: 31862608]

Lim IAL, Faria AV, Li X, Hsu JTC, Airan RD, Mori S, van Ziji PCM, 2013. Human brain atlas for automated region of interest selection in quantitative susceptibility mapping: application to determine iron content in deep gray matter structures. Neuroimage 82, 449–469. [PubMed: 23769915]

Lin CP, Tseng WYI, Cheng HC, Chen JH, 2001. Validation of diffusion tensor magnetic resonance axonal fiber imaging with registered manganese-enhanced optic tracts. Neuroimage 14, 1035–1047. [PubMed: 11697935]

Lin Z, Gong T, Wang K, Li Z, He H, Tong Q, Yu F, Zhong J, 2019. Fast learning of fiber orientation distribution function for MR tractography using convolutional neural network. Med. Phys 46, 3101–3116. [PubMed: 31009085]

Lo CY, Wang PN, Chou KH, Wang J, He Y, Lin CP, 2010. Diffusion tensor tractography reveals abnormal topological organization in structural cortical networks in Alzheimer's disease. J. Neurosci 30, 16876–16885. [PubMed: 21159959]

Maier-Hein KH, Neher PF, Houde JC, Cote MA, Garyfallidis E, Zhong J, Chamberland M, Yeh FC, Lin YC, Ji Q, Reddick WE, Glass JO, Chen DQ, Feng Y, Gao C, Wu Y, Ma J, He R, Li Q, Westin CF, Deslauriers-Gauthier S, Gonzalez JOO, Paquette M, St-Jean S, Girard G, Rheault F, Sidhu J, Tax CMW, Guo F, Mesri HY, David S, Froeling M, Heemskerk AM, Leemans A, Bore A, Pinsard B, Bedetti C, Desrosiers M, Brambati S, Doyon J, Sarica A, Vasta R, Cerasa A, Quattrone A, Yeatman J, Khan AR, Hodges W, Alexander S, Romascano D, Barakovic M, Auria A, Esteban O, Lemkaddem A, Thiran JP, Cetingul HE, Odry BL, Mailhe B, Nadar MS, Pizzagalli F, Prasad G, Villalon-Reina JE, Galvis J, Thompson PM, Requejo FS, Laguna PL, Lacerda LM, Barrett R, Dell'Acqua F, Catani M, Petit L, Caruyer E, Daducci A, Dyrby TB, Holland-Letz T, Hilgetag CC, Stieltjes B, Descoteaux M, 2017. The challenge of mapping the human connectome based on diffusion tractography. Nat. Commun 8, 1349. [PubMed: 29116093]

McFarland NR, Lee JS, Hyman BT, McLean PJ, 2009. Comparison of transduction efficiency of recombinant AAV serotypes 1, 2, 5, and 8 in the rat nigrostriatal system. J. Neurochem 109, 838–845. [PubMed: 19250335]

Miller MI, Trouve A, Younes L, 2002. On the metrics and euler-lagrange equations of computational anatomy. Annu. Rev. Biomed. Eng 4, 375–405. [PubMed: 12117763]

Moldrich RX, Pannek K, Hoch R, Rubenstein JL, Kurniawan ND, Richards LJ, 2010. Comparative mouse brain tractography of diffusion magnetic resonance imaging. Neuroimage 51, 1027–1036. [PubMed: 20303410]

Mollink J, Kleinnijenhuis M, Cappellen van Walsum AV, Sotiropoulos SN, Cottaar M, Mirfin C, Heinrich MP, Jenkinson M, Pallebage-Gamarallage M, Ansorge O, Jbabdi S, Miller KL, 2017. Evaluating fibre orientation dispersion in white matter: comparison of diffusion MRI, histology and polarized light imaging. Neuroimage 157, 561–574. [PubMed: 28602815]

Mori S, van Zijl PC, 2002. Fiber tracking: principles and strategies - a technical review. NMR Biomed. 15, 468–480. [PubMed: 12489096]

Nath V, Schilling KG, Parvathaneni P, Hansen CB, Hainline AE, Huo Y, Blaber JA, Lyu I, Janve V, Gao Y, Stepniewska I, Anderson AW, Landman BA, 2019. Deep learning reveals untapped information for local white-matter fiber reconstruction in diffusion-weighted MRI. Magn. Reson. Imaging 62, 220–227. [PubMed: 31323317]

Oh SW, Harris JA, Ng L, Winslow B, Cain N, Mihalas S, Wang QX, Lau C, Kuan L, Henry AM, Mortrud MT, Ouellette B, Nguyen TN, Sorensen SA, Slaughterbeck CR, Wakeman W, Li Y, Feng D, Ho A, Nicholas E, Hirokawa KE, Bohn P, Joines KM, Peng HC, Hawrylycz MJ, Phillips JW, Hohmann JG, Wohnoutka P, Koch C, Bernard A, Dang C, Jones AR, Zeng HK, Gerfen CR, 2014. A mesoscale connectome of the mouse brain. Nature 508, 207 - +. [PubMed: 24695228]

Poot DH, Jeurissen B, Bastiaensen Y, Veraart J, Van Hecke W, Parizel PM, Sijbers J, 2013. Super-resolution for multislice diffusion tensor imaging. Magn. Reson. Med 69, 103–113. [PubMed: 22411778]

Ren T, Zhang J, Plachez C, Mori S, Richards LJ, 2007. Diffusion tensor magnetic resonance imaging and tract-tracing analysis of Probst bundle structure in Netrin1- and DCC-deficient mice. J. Neurosci 27, 10345–10349. [PubMed: 17898206]

Reveley C, Seth AK, Pierpaoli C, Silva AC, Yu D, Saunders RC, Leopold DA, Ye FQ, 2015. Superficial white matter fiber systems impede detection of long-range cortical connections in diffusion MR tractography. Proc. Natl. Acad. Sci. U. S. A 112, E2820–E2828. [PubMed: 25964365]

Rheault F, Poulin P, Valcourt Caron A, St-Onge E, Descoteaux M, 2020. Common misconceptions, hidden biases and modern challenges of dMRI tractography. J. Neural Eng 17, 011001. [PubMed: 31931484]

Scheffer LK, Xu CS, Januszewski M, Lu Z, Takemura SY, Hayworth KJ, Huang GB, Shinomiya K, Maitlin-Shepard J, Berg S, Clements J, Hubbard PM, Katz WT, Umayam L, Zhao T, Ackerman D, Blakely T, Bogovic J, Dolafi T, Kainmueller D, Kawase T, Khairy KA, Leavitt L, Li PH, Lindsey L, Neubarth N, Olbris DJ, Otsuna H, Trautman ET, Ito M, Bates AS, Goldammer J, Wolff T, Svirskas R, Schlegel P, Neace E, Knecht CJ, Alvarado CX, Bailey DA, Ballinger S, Borycz JA, Canino BS, Cheatham N, Cook M, Dreher M, Duclos O, Eubanks B, Fairbanks K, Finley S, Forknall N, Francis A, Hopkins GP, Joyce EM, Kim S, Kirk NA, Kovalyak J, Lauchie SA, Lohff A, Maldonado C, Manley EA, McLin S, Mooney C, Ndama M, Ogundeyi O, Okeoma N, Ordish C, Padilla N, Patrick CM, Paterson T, Phillips EE, Phillips EM, Rampally N, Ribeiro C, Robertson MK, Rymer JT, Ryan SM, Sammons M, Scott AK, Scott AL, Shinomiya A, Smith C, Smith K, Smith NL, Sobeski MA, Suleiman A, Swift J, Take mura S, Talebi I, Tarnogorska D, Tenshaw E, Tokhi T, Walsh JJ, Yang T, Horne JA, Li F, Parekh R, Rivlin PK, Jayaraman V, Costa M, Jefferis GS, Ito K, Saalfeld S, George R, Meinertzhagen IA, Rubin GM, Hess HF, Jain V, Plaza SM, 2020. A connectome and analysis of the adult Drosophila central brain. eLife 9.

Schilling K, Janve V, Gao Y, Stepniewska I, Landman BA, Anderson AW, 2016. Comparison of 3D orientation distribution functions measured with confocal microscopy and diffusion MRI. Neuroimage 129, 185–197. [PubMed: 26804781]

Schilling KG, Janve V, Gao Y, Stepniewska I, Landman BA, Anderson AW, 2018. Histological validation of diffusion MRI fiber orientation distributions and dispersion. Neuroimage 165, 200–221. [PubMed: 29074279]

Schilling KG, Nath V, Hansen C, Parvathaneni P, Blaber J, Gao YR, Neher P, Aydogan DB, Shi YG, Ocampo-Pineda M, Schiavi S, Daducci A, Girard G, Barakovic M, Rafael-Patino J, Romascano D, Rensonnet G, Pizzolato M, Bates A, Fischi E, Thiran JP, Canales-Rodriguez EJ, Huang C, Zhu HT, Zhong LM, Cabeen R, Toga AW, Rheault F, Theaud G, Houde JC, Sidhu J, Chamberland M, Westin CF, Dyrby TB, Verma R, Rathi Y, Irfanoglu MO, Thomas C, Pierpaoli C, Descoteaux M, Anderson AW, Landman BA, 2019. Limits to anatomical accuracy of diffusion tractography using modern approaches. Neuroimage 185, 1–11. [PubMed: 30317017]

Schurr R, Duan YR, Norcia AM, Ogawa S, Yeatman JD, Mezer AA, 2018. Tractography optimization using quantitative T1 mapping in the human optic radiation. Neuroimage 181, 645–658. [PubMed: 29936310]

Seehaus AK, Roebroeck A, Chiry O, Kim DS, Ronen I, Bratzke H, Goebel R, Galuske RA, 2013. Histological validation of DW-MRI tractography in human postmortem tissue. Cereb. Cortex 23, 442–450. [PubMed: 22345356]

Srivastava N, Hinton G, Krizhevsky A, Sutskever I, Salakhutdinov R, 2014. Dropout: a simple way to prevent neural networks from overfitting. J. Mach. Learn. Res 15, 1929–1958.

Thomas C, Ye FQ, Irfanoglu MO, Modi P, Saleem KS, Leopold DA, Pierpaoli C, 2014. Anatomical accuracy of brain connections derived from diffusion MRI tractography is inherently limited. Proc. Natl. Acad. Sci. U. S. A 111, 16574–16579. [PubMed: 25368179]

Topgaard D, 2017. Multidimensional diffusion MRI. J. Magn. Reson 275, 98–113. [PubMed: 28040623]

Tournier JD, Calamante F, Connelly A, 2007. Robust determination of the fibre orientation distribution in diffusion MRI: non-negativity constrained super-resolved spherical deconvolution. Neuroimage 35, 1459–1472. [PubMed: 17379540]

Tournier JD, Smith R, Raffelt D, Tabbara R, Dhollander T, Pietsch M, Christiaens D, Jeurissen B, Yeh CH, Connelly A, 2019. MRtrix3: a fast, flexible and open software framework for medical image processing and visualisation. Neuroimage 202.

Tuch DS, Reese TG, Wiegell MR, Makris N, Belliveau JW, Wedeen VJ, 2002. High angular resolution diffusion imaging reveals intravoxel white matter fiber heterogeneity. Magn. Reson. Med 48, 577–582. [PubMed: 12353272]

Wang K, Tamir JI, De Goyeneche A, Wollner U, Brada R, Yu SX, Lustig M, 2022. High fidelity deep learning-based MRI reconstruction with instance-wise discriminative feature matching loss. Magn. Reson. Med 88, 476–491. [PubMed: 35373388]

Wedeen VJ, Rosene DL, Wang RP, Dai GP, Mortazavi F, Hagmann P, Kaas JH, Tseng WYI, 2012. The geometric structure of the brain fiber pathways. Science 335, 1628–1634. [PubMed: 22461612]

Wedeen VJ, Wang RP, Schmahmann JD, Benner T, Tseng WY, Dai G, Pandya DN, Hagmann P, D'Arceuil H, de Crespigny AJ, 2008. Diffusion spectrum magnetic resonance imaging (DSI) tractography of crossing fibers. Neuroimage 41, 1267–1277. [PubMed: 18495497]

White JD, Arefin TM, Pugliese A, Lee CH, Gassen J, Zhang JY, Kaffman A, 2020. Early life stress causes sex-specific changes in adult fronto-limbic connectivity that differentially drive learning. eLife 9.

Winnubst J, Bas E, Ferreira TA, Wu Z, Economo MN, Edson P, Arthur BJ, Bruns C, Rokicki K, Schauder D, Olbris DJ, Murphy SD, Ackerman DG, Arshadi C, Baldwin P, Blake R, Elsayed A, Hasan M, Ramirez D, Dos Santos B, Weldon M, Zafar A, Dudman JT, Gerfen CR, Hantman AW, Korff W, Sternson SM, Spruston N, Svoboda K, Chandrashekar J, 2019. Reconstruction of 1,000 projection neurons reveals new cell types and organization of long-range connectivity in the mouse brain. Cell 179, 268–281 e213. [PubMed: 31495573]

Wu D, Reisinger D, Xu JD, Fatemi SA, van Zijl PCM, Mori S, Zhang JY, 2014. Localized diffusion magnetic resonance micro-imaging of the live mouse brain. Neuroimage 91, 12–20. [PubMed: 24440780]

Wu D, Xu J, McMahon MT, van Zijl PC, Mori S, Northington FJ, Zhang J, 2013. *In vivo* high-resolution diffusion tensor imaging of the mouse brain. Neuroimage 83, 18–26. [PubMed: 23769916]

Wu D, Zhang JY, 2016. *In vivo* mapping of macroscopic neuronal projections in the mouse hippocampus using high-resolution diffusion MRI. Neuroimage 125, 84–93. [PubMed: 26499812]

Xu F, Shen Y, Ding L, Yang CY, Tan H, Wang H, Zhu Q, Xu R, Wu F, Xiao Y, Xu C, Li Q, Su P, Zhang LI, Dong HW, Desimone R, Xu F, Hu X, Lau PM, Bi GQ, 2021. High-throughput mapping of a whole rhesus monkey brain at micrometer resolution. Nat. Biotechnol 39, 1521–1528. [PubMed: 34312500]

Ying X, 2019. An overview of overfitting and its solutions. In: Proceedings of the 2018 International Conference on Computer Information Science and Application Technology 1168.

Zingg B, Hintiryan H, Gou L, Song MY, Bay M, Bienkowski MS, Foster NN, Yamashita S, Bowman I, Toga AW, Dong HW, 2014. Neural networks of the mouse neocortex. Cell 156, 1096–1111. [PubMed: 24581503]

Zur RM, Jiang YL, Pesce LL, Drukker K, 2009. Noise injection for training artificial neural networks: a comparison with weight decay and early stopping. Med. Phys 36, 4810–4818. [PubMed: 19928111]

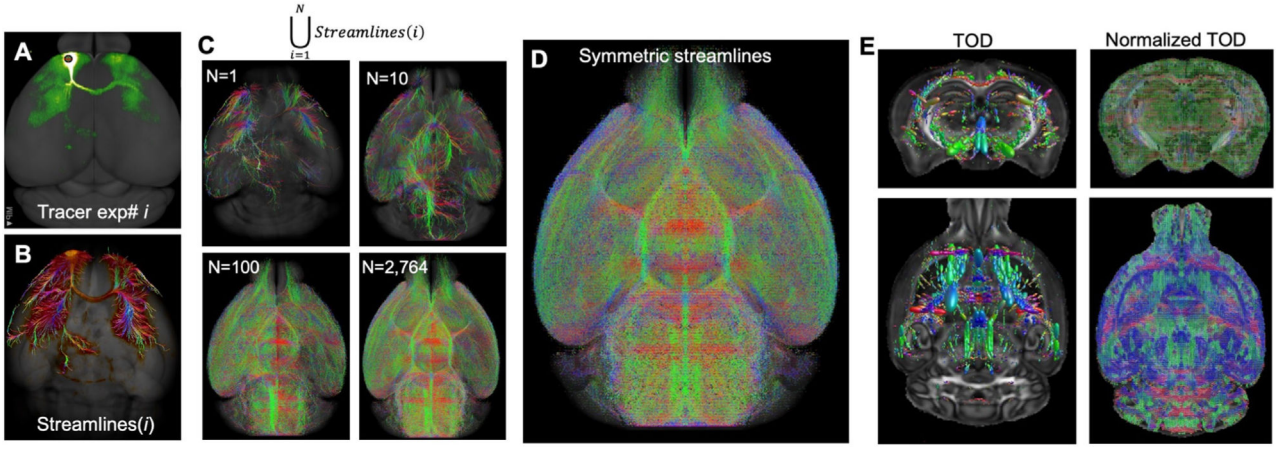

Fig. 1.

Generation of the aggregated AMBCA streamlines. A-B: A representative tracer experiment (ID# 100140756, injected in frontal pole) and its corresponding single-experiment (SE) AMBCA streamlines generated using a fast-marching algorithm. C: The process of adding streamlines from all 2764 injection experiments, with injection sites mainly located in one hemisphere. D: A symmetric 4-million streamline dataset was generated by mirroring the streamlines in C with respect to the mid-sagittal plane and added to the result in C. E: (TOD) maps generated from the aggregated AMBCA streamlines and after amplitude normalization.

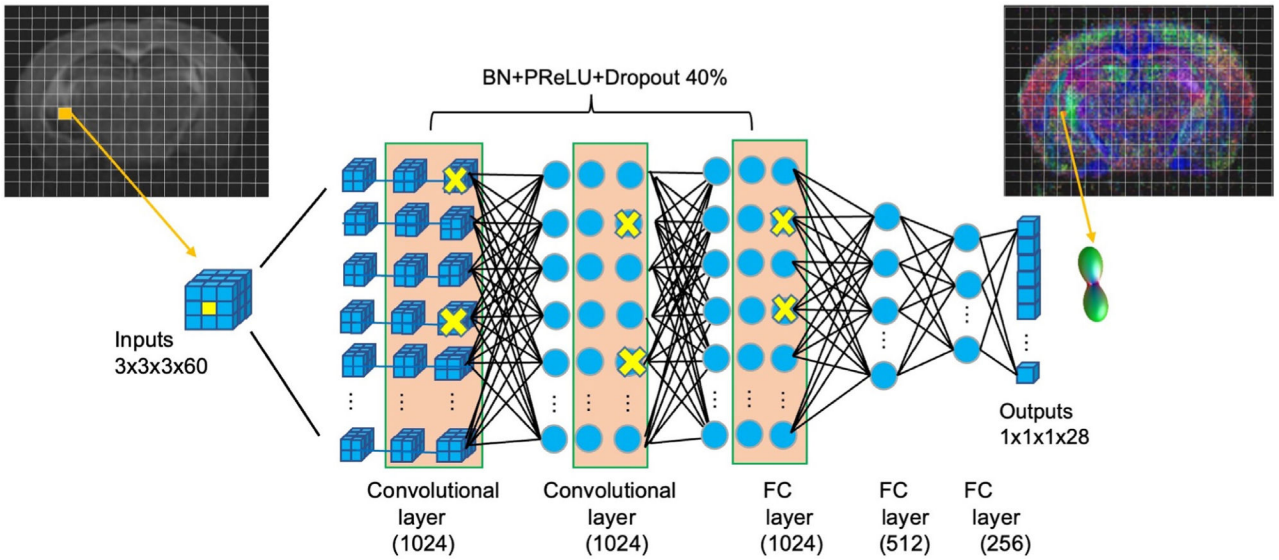

Fig. 2.

The basic architecture of TODNet. The inputs to the network were 3 × 3 × 3 voxel patches containing diffusion-weighted signals along 60 diffusion encoding directions from the voxels normalized by non-diffusion-weighted signals. The outputs were TODs with 28 spherical harmonic coefficients. The network contained 5 layers with 1024, 1024, 1024, 512, 256 output neurons, represented by the blue dots. In the first three layers, 40% neurons were dropped-off for regularization as indicated by yellow “X ”.

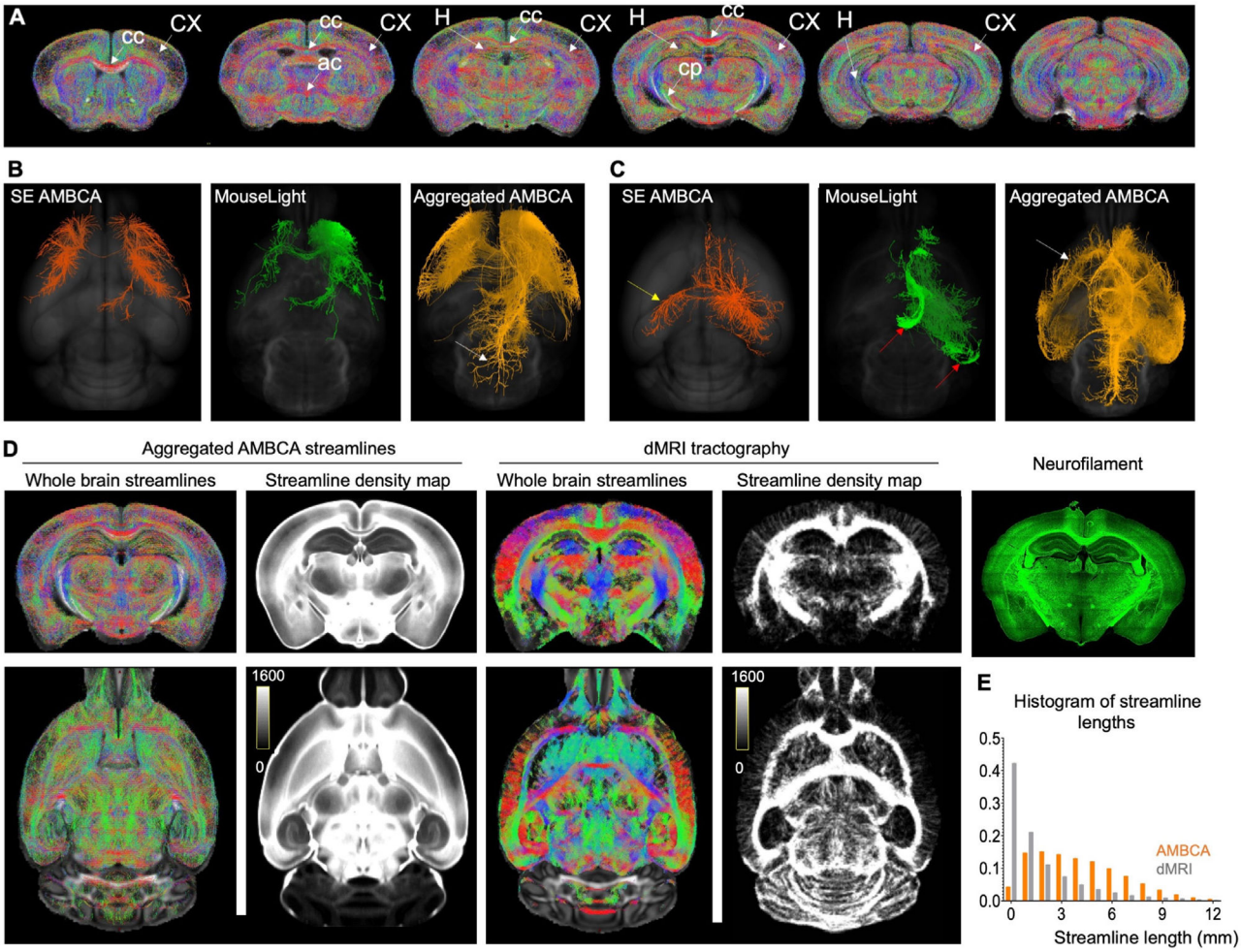

Fig. 3.

Axonal pathways in the aggregated AMBCA streamlines and comparisons with dMRI tractography. A: Axonal networks in the mouse brain shown in serial coronal sections of the aggregated AMBCA streamlines. Abbreviations: ac: anterior commissure; cc: corpus callosum; cp: cerebral peduncle; CX: cortex; H: hippocampus. B-C: A comparison of SE AMBCA streamlines originated from an injection site in the frontal cortex (B) and hippocampus (C) and streamlines in the aggregated MouseLight and AMBCA streamlines that passed the same injection site. In (C), the SE AMBCA streamlines reached the contralateral hemisphere (indicated by the yellow arrow), while the selected MouseLight streamlines showed more axonal pathways in the ipsilateral hemisphere (indicated by the red arrows). The white arrows in (B) and (C) indicate the additional streamlines found in the aggregated AMBCA streamlines. D: Comparisons of aggregated AMBCA and whole brain dMRI tractography streamlines acquired in this study and corresponding streamline density maps, with a matching Neurofilament-stained section from the Allen reference atlas. E: The histograms of streamline lengths in the AMBCA and dMRI tractography results.

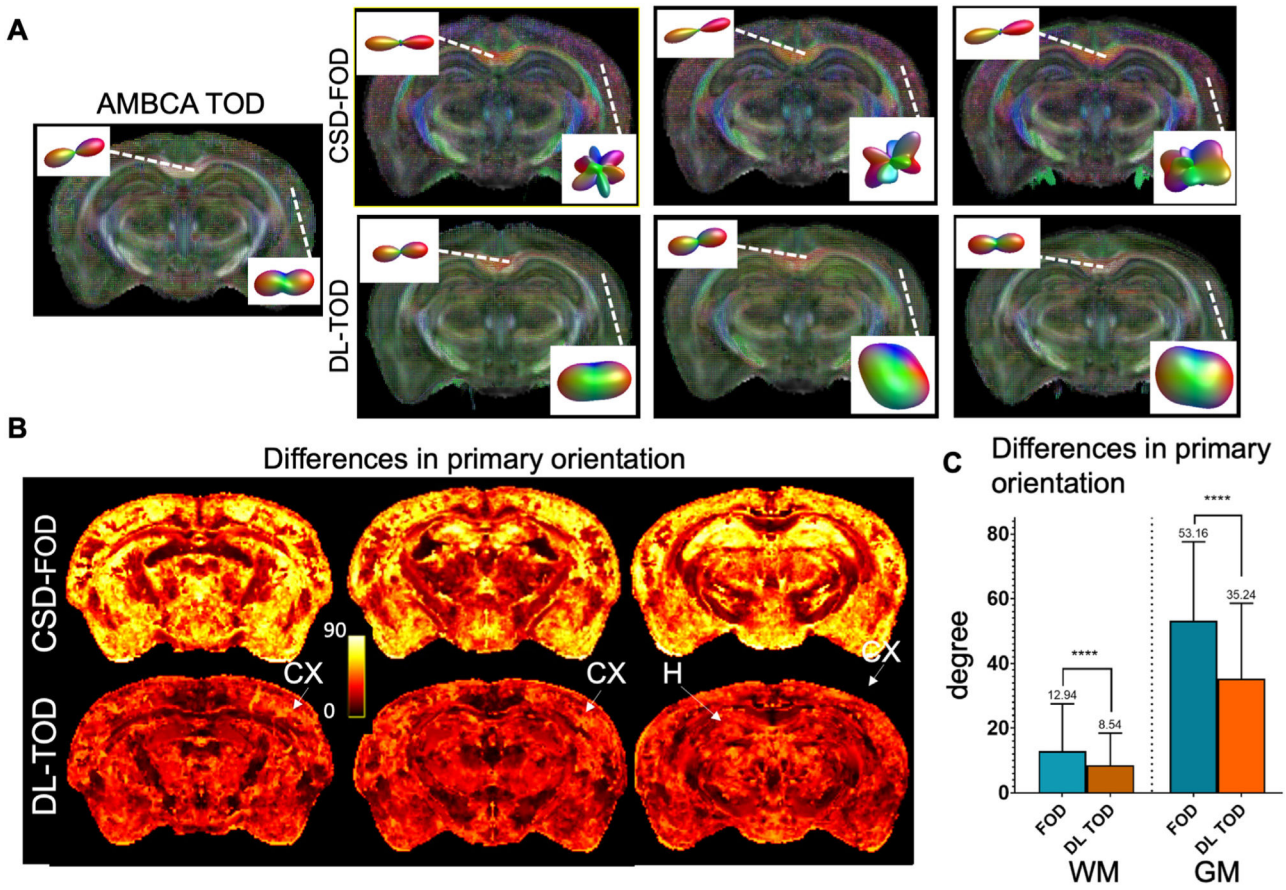

Fig. 4.

Comparisons of DL-TOD and CSD-FOD. A: The estimated DL-TOD and CSD-FOD maps from three mouse brains not included in training. B: The average differences in the primary orientation in degree between the DL-TODs and AMBCA TODs and between the CSD-FODs and AMBCA TODs in the mouse brain data not included in training ($n = 4$). Notice the reductions in primary orientation differences in the cortex (CX) and hippocampus (H) in the DL-TOD results compared to the CSD-FOD results. C: Differences in primary orientation in white matter (WM) and gray matter (GM) in degree. * * * * indicates $p < 0.0001$.

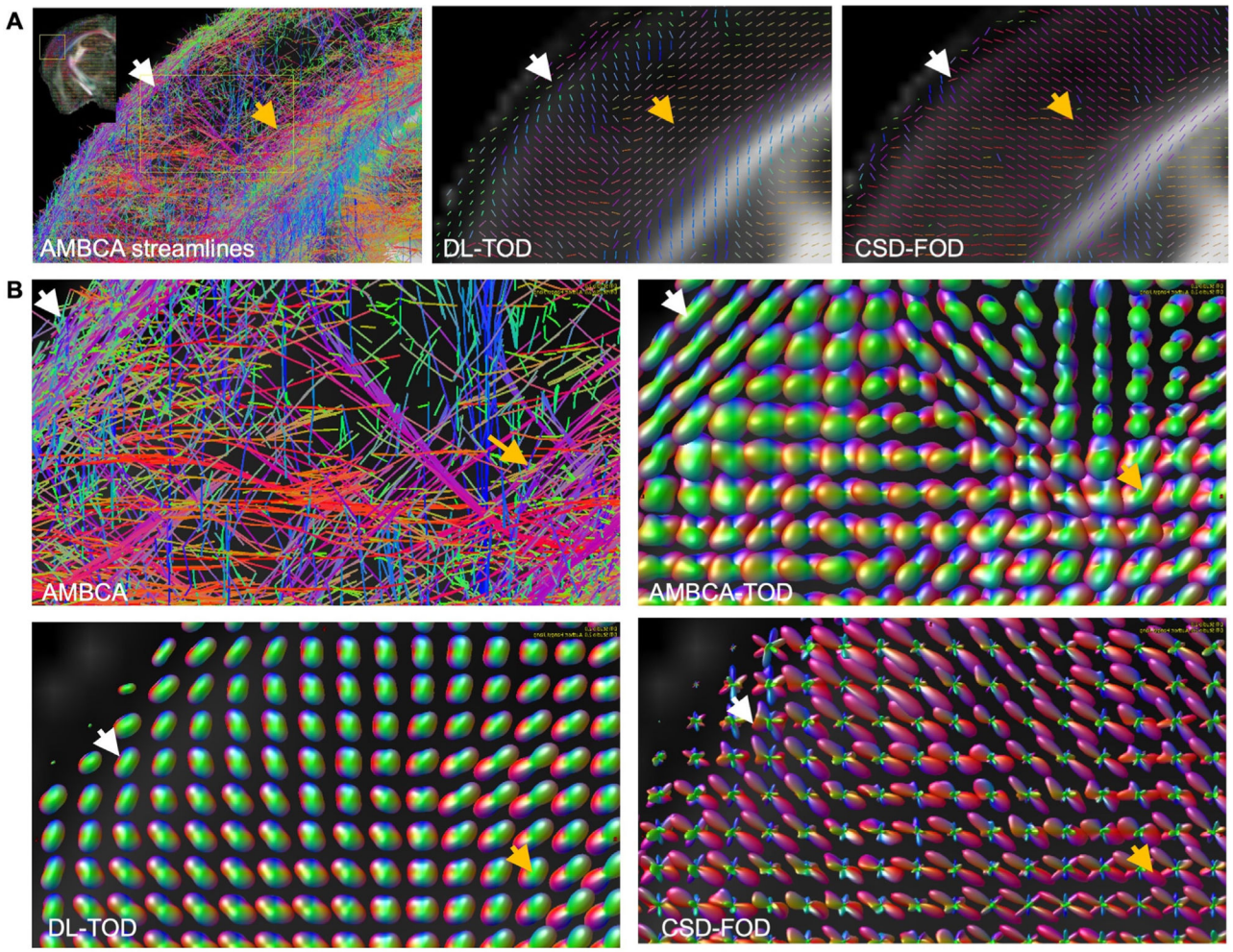

Fig. 5.

DL-TOD maps recapitulated axonal networks in the cortex. A: The aggregated AMBCA streamlines in the sensory cortex (its location is shown in the insert) were compared with the primary orientations of DL-TODs and CSD-FODs. The white and orange arrows indicate the superficial and deep regions of the cortex, where the primary orientation of DL-TODs and CSD-FODs differed. B: AMBCA TODs were compared with DL-TODs and CSD-FODs in the same region.

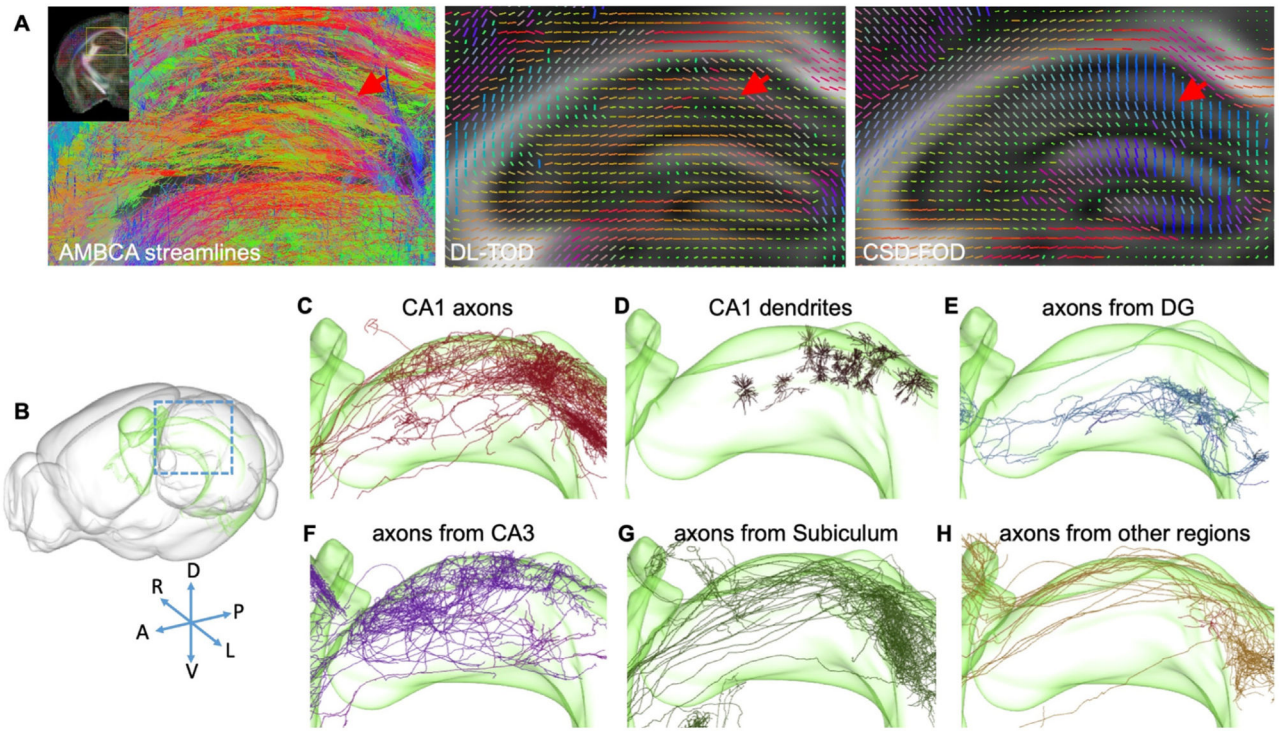

Fig. 6.

DL-TOD maps recapitulated axonal networks in the hippocampus. A: Aggregated AMBCA streamlines in the dorsal hippocampus (its location is shown in the insert) were compared with the primary orientations of DL-TODs and CSD-FODs. The red arrow indicates a group of streamlines running in the horizontal orientation (red), which were found in the primary orientation map of DL-TODs but not in the CSD-FODs. B-H: Visualization of axonal and dendritic networks in the hippocampus CA1 region within the hippocampus (the green surface in the mouse brain, B) based on selected cell tracing results from the MouseLight project (http://ml-neuronbrowser.janelia.org/), including axons and dendrites from CA1 neurons (C-D) as well as axons in the CA1 region but originated from other parts of the hippocampus (E-H) DG is the abbreviation of dentate gyrus.

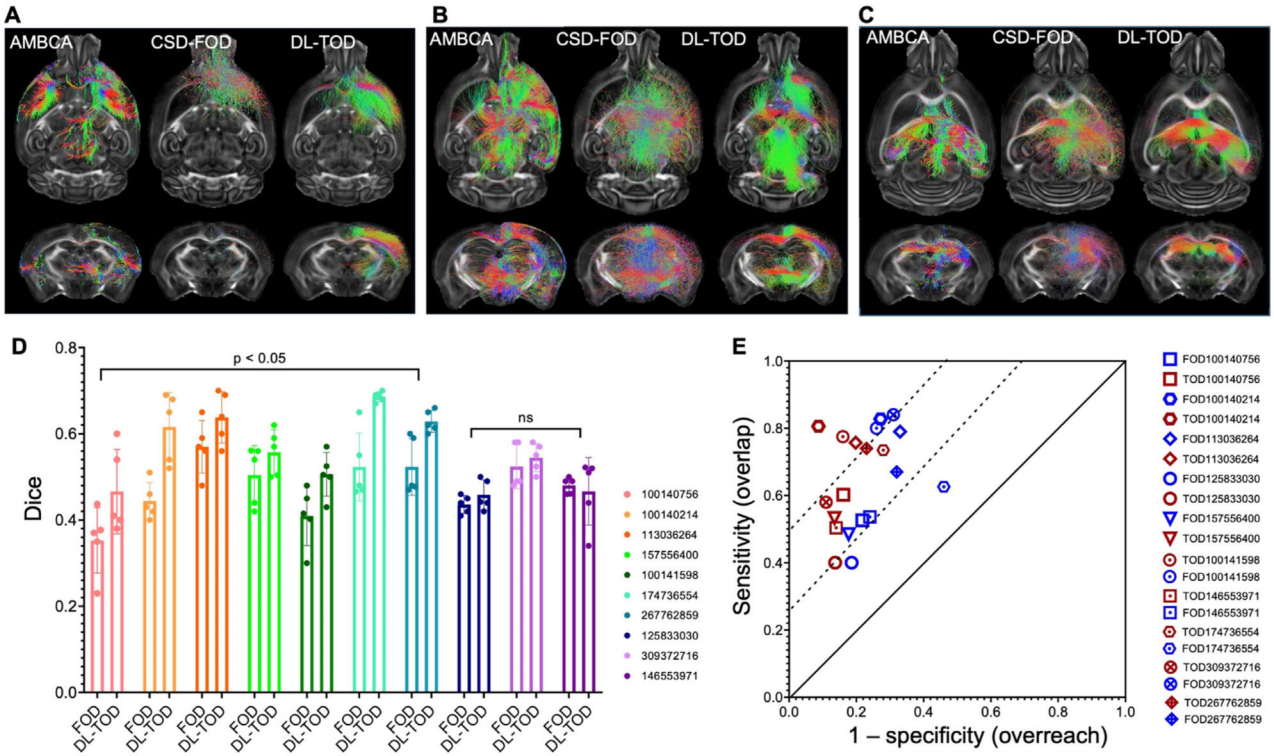

Fig. 7.

DL-TODs improved dMRI tractography in the mouse brain. A-C: Comparisons of streamlines selected from the AMBCA streamline dataset and CSD-FOD/DL-TOD based tractography using injection regions in the frontal cortex (A), thalamus (B), and hippocampus (C). D: Spatial overlaps between streamlines selected from the AMBCA streamline dataset and CSD-FOD/DL-TOD based tractography using 10 injection sites in AMBCA measured using DICE. E: For the results in E, DL-TOD based tractography results tended to have higher specificity (smaller overreach) than CSD-FOD based tractography results while maintaining similar sensitivity (overlap).

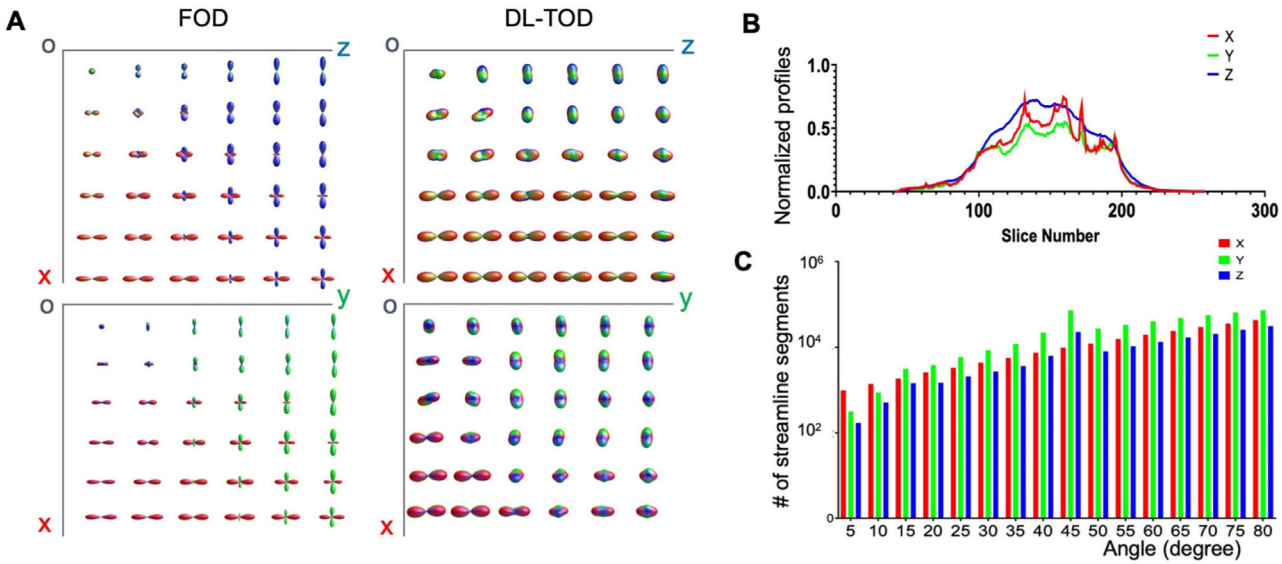

Fig. 8.

Comparing CSD-FODs and DL-TODs in a digital phantom and potential bias in the AMBCA streamline database. A: Estimated FODs and TODs from a digital phantom containing both single and orthogonal crossing fiber configurations (top: X and Y; bottom: X and Z). B: The normalized profiles of AMBCA streamline segments along the X, Y, and Z axes in each axial slice. C: The distributions of angles between each AMBCA streamline segments and the three axes.

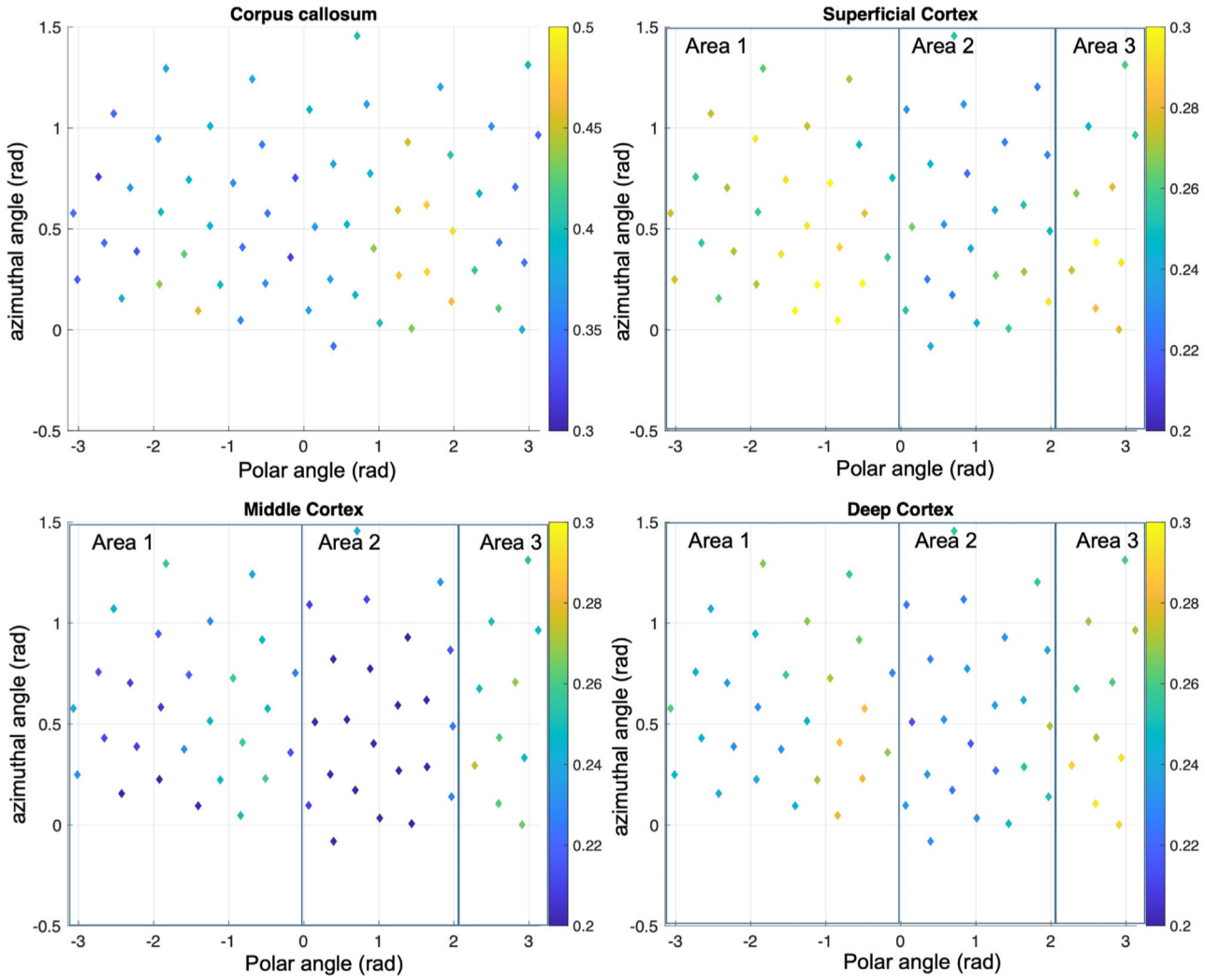

Fig. 9.

Normalized dMRI signals from representative voxels in the corpus callosum, superficial, middle, and deep cortical regions. The locations of the signals in the plot indicate the polar and azimuthal angles of the corresponding diffusion encoding gradient, and the color indicates the normalized signal strength (with respect to non-diffusion-weighted signals). The plots of cortical dMRI signals are overlaid with three rectangular boxes (areas 1–3) to guide visual comparisons.

Table 1

The eigen-values of D_1 and D_2 in the digital phantom for X-Y and X-Z crossing fiber configurations. The unit of the eigen-value is $\mu m^2/ms$.

X-	D_1	0.14, 0.14, 0.14	0.18, 0.12, 0.12	0.22, 0.10, 0.10	0.26, 0.08, 0.08	0.30, 0.06, 0.06	0.34, 0.04, 0.04
Y	D_2	0.14, 0.14, 0.14	0.12, 0.18, 0.12	0.10, 0.22, 0.10	0.08, 0.26, 0.08	0.06, 0.30, 0.06	0.04, 0.34, 0.04
X-	D_1	0.14, 0.14, 0.14	0.18, 0.12, 0.12	0.22, 0.10, 0.10	0.26, 0.08, 0.08	0.30, 0.06, 0.06	0.34, 0.04, 0.04
Z	D_2	0.14, 0.14, 0.14	0.12, 0.12, 0.18	0.10, 0.10, 0.22	0.08, 0.08, 0.26	0.06, 0.06, 0.30	0.04, 0.04, 0.34